processes

MDPI

Article

Liquid–Solid Coupled Internal Flow Field Analysis of Natural Gas Hydrate Spiral-Swirling Downhole In Situ Separator

Yufa He [1], Xiaohui Jiang [2,3], Yang Tang [2,3,4,*], Yunjian Zhou [1], Na Xie [2,3] and Guorong Wang [2,3,4]

[1] State Key Laboratory of Offshore Natural Gas Hydrates, CNOOC Research Institute Ltd., Beijing 100028, China; heyf@cnooc.com.cn (Y.H.); zcx123tt@163.com (Y.Z.)
[2] School of Mechatronic Engineering, Southwest Petroleum University, Chengdu 610500, China; jxh286464094@126.com (X.J.); xn18141359930@126.com (N.X.); swpi2002@163.com (G.W.)
[3] Energy Equipment Institute, Southwest Petroleum University, Chengdu 610500, China
[4] Sichuan Science and Technology Resources Sharing Service Platform, Chengdu 610500, China
* Correspondence: tangyanggreat@126.com

Abstract: This study aims to solve the problem of the recovery efficiency of natural gas hydrate being affected by a large amount of mud and sand in the solid fluidization mining of natural gas hydrate. Therefore, a new method for the separation of in situ sediment and natural gas hydrate in a spiral-swirling downhole is proposed, and the corresponding numerical simulation model is established to realize the analysis and verification of key flow field parameters such as flow velocity, pressure, sediment, and natural gas hydrate phase distribution. The results show that the flow velocity field of the mixed slurry presents an 'M'-shaped symmetrical distribution, and the slurry near the wall of the separator can obtain a larger flow velocity, which is beneficial to the separation of mud–sand and natural gas hydrate. The static pressure field shows an axisymmetric distribution that decreases first and then increases, indicating that the pressure of the mixed slurry increases with the increase in the radial position, and the closer to the wall, the greater the static pressure of the mixed slurry. Near the wall of the separator, the volume fraction of the sediment phase reaches the maximum. In contrast, the volume fraction of the natural gas hydrate phase reaches the minimum, which confirms the separation effect of the sediment and the natural gas hydrate. The results show that the separation of sediments and natural gas hydrate can be realized, thereby improving the exploitation efficiency of natural gas hydrate. The designed spiral cyclone coupling separator provides a new solution to solving the problem of sand removal in natural gas hydrate exploitation.

Keywords: natural gas hydrate; separator; spiral-swirl coupling; numerical simulation flow; field analysis; mud–sand separation

check for updates

Academic Editor: Ali Hassanpour

Received: 3 December 2024
Revised: 12 January 2025
Accepted: 22 January 2025
Published: 28 January 2025

Citation: He, Y.; Jiang, X.; Tang, Y.; Zhou, Y.; Xie, N.; Wang, G. Liquid–Solid Coupled Internal Flow Field Analysis of Natural Gas Hydrate Spiral-Swirling Downhole In Situ Separator. *Processes* **2025**, *13*, 360. https://doi.org/10.3390/pr13020360

Copyright: © 2025 by the authors. Licensee MDPI, Basel, Switzerland. This article is an open access article distributed under the terms and conditions of the Creative Commons Attribution (CC BY) license (https://creativecommons.org/licenses/by/4.0/).

1. Introduction

Natural gas hydrate (NGH), often termed 'combustible ice', is recognized as a promising clean energy source due to its extensive reserves. Estimates indicate that the global reserves of methane within natural gas hydrate resources amount to approximately 3×10^{15} m^3 [1–3]. In the quest for carbon neutrality, natural gas hydrates are emerging as a viable and eco-friendly fuel, potentially bridging the gap between renewable energy supply and demand [4]. Current extraction methods include depressurization, CO_2 replacement, chemical inhibitors, and thermal excitation [5–9]. However, these methods face wellbore safety hazards, production control, and environmental risks. A downhole in situ separation technology based on solid fluidization has been developed to overcome these issues, showing promising results in trials in the South China Sea [10,11]. This process involves using

a high-pressure water jet to disintegrate the hydrate reservoir, creating a hydrate slurry. The slurry is then processed by a downhole separation device integrated into the pipeline, with the purified natural gas hydrate being pumped to the surface for controlled decomposition. The effective separation of mud and sand from the hydrate slurry is therefore essential [12,13]. However, the process of natural gas hydrate exploitation faces a problem, in that a large amount of sand production leads to the termination of production tests; these mud–sands are mostly silt, with a large particle size span, and some of the mud–sand particle sizes reach micron level. Most of the existing separators are cyclone separators or spiral separators. Cyclone separators have high separation efficiency [14], but are poor at separating particles with a particle size of 1~10 μm [15]. The spiral separator also has a good separation effect on small particles [16–20].

Based on this, our team has developed an innovative spiral-swirl coupling separator [21]. However, the existing research on the velocity, pressure, and other parameters in the internal flow field of the separator is not clear. These factors are crucial in the separation process and significantly influence the final performance of the separator. Xie [22] proposed a new type of cyclone separator and cylinder filter and analyzed the separation performance of the separator, but the flow field characteristics such as internal velocity and pressure were not studied. Lan et al. proposed a downhole gas–liquid separator specifically designed for natural gas hydrates and explored its use for efficient downhole sand removal [23]. This device operates as a spiral separator and employs an electric submersible pump (ESP) to facilitate its function. Nie investigated the safety performance of downhole solid–liquid separators subjected to torsional stress conditions [24]. Expanding on existing models, Qiu offered a comprehensive analysis of the influence of reservoir parameters on the behavior of spiral separators [25]. Chang explored the effects of operational and geometric parameters on hydrocyclone performance through both experimental methods and computational fluid dynamics (CFD) simulations [26–28]. Foroozesh et al. used CFD technology and Ansys-Fluent 19.2 software to study the influence of wall roughness of cyclone separator on cyclone erosion rate and cyclone performance and used the Reynolds stress transfer model to simulate airflow turbulence in cyclone rotating airflow [29]. Singh et al. used the computational fluid dynamics method to simulate the complex solid–liquid flow of coal water slurry on the divergent section of the cyclone separator cone and carried out experimental verification. The experimental results show that the simulation results of the cyclone separator are correct [30].

The research on the flow field characteristics of the spiral-swirl coupling separator is at the forefront of research in this field, and the flow field of the spiral-swirl coupling separator is different from the flow field of the traditional hydro cyclone, which is still unclear. The purpose of this study is to reveal the flow field characteristics of the swirl coupling separator. The flow field numerical simulation of the spiral-swirl in situ separator was carried out. The particle trajectory of the spiral-swirl flow channel was verified by discrete element numerical simulation analysis. The velocity field, pressure field, mud–sand phase, and natural gas hydrate phase distribution of the spiral-swirl in situ separator were analyzed. The axial velocity distribution, radial velocity distribution, tangential velocity distribution, static pressure distribution, mud–sand phase distribution, hydrate phase distribution, and other parameters were obtained. Finally, the study shows that the spiral-swirl coupling separator has a good effect on the separation of mud and sand in the natural gas hydrate.

2. Geometric Model

2.1. Numerical Calculation Model

2.1.1. Fluid Control Equation

Material flow behavior adheres to the fundamental principles of classical fluid mechanics, which govern mass and momentum conservation. The liquid phase is treated as a viscous, incompressible fluid within the separator. Below are the continuity and momentum equations applicable to steady, laminar, incompressible, isothermal, and axisymmetric flow conditions [31,32].

$$\frac{\mathrm{d}\rho}{\mathrm{d}t} + \rho\frac{\partial u_i}{\partial x_i} = 0 \tag{1}$$

where ρ is the fluid phase density. u_i is the velocity in the l direction. x_i is the position in the I direction. t is the fluid time. $d\rho/dt$ is the derivative of the fluid phase density relative to time, which distinguishes compressible and incompressible fluids. In the numerical simulation of hydrate mixed slurry in this paper, the fluid is generally considered incompressible, so $d\rho/dt = 0$.

The fluid momentum conservation equation is as follows:

$$\begin{cases} v\frac{\partial w}{\partial r} + w\frac{\partial w}{\partial z} = -\frac{1}{\rho}\frac{\partial p}{\partial z} + \frac{\mu}{\rho}\left[\frac{1}{r}\frac{\partial}{\partial r}\left(r\frac{\partial w}{\partial r}\right) + \frac{\partial^2 w}{\partial z^2}\right] \\ v\frac{\partial v}{\partial r} + w\frac{\partial v}{\partial z} - \frac{u^2}{r} = -\frac{1}{\rho}\frac{\partial p}{\partial r} + \frac{\mu}{\rho}\left[\frac{1}{r}\frac{\partial}{\partial r}\left(r\frac{\partial v}{\partial r}\right) + \frac{\partial^2 v}{\partial z^2} - \frac{v}{r^2}\right] \\ v\frac{\partial u}{\partial r} + w\frac{\partial u}{\partial z} + \frac{vu}{r} = \frac{\mu}{\rho}\left[\frac{1}{r}\frac{\partial}{\partial r}\left(r\frac{\partial u}{\partial r}\right) + \frac{\partial^2 u}{\partial z^2} - \frac{u}{r^2}\right] \end{cases} \tag{2}$$

where u, v, and w represent axial, radial, and tangential, respectively. p is the pressure. k is the turbulent kinetic energy. ε is the turbulent kinetic energy dissipation rate.

2.1.2. Turbulence Modeling

The spiral-swirl coupling in situ separator developed in this study bears similarities to a conventional hydrocyclone. It generally functions within a turbulent regime during the centrifugal separation of multiphase flows. A variety of turbulence models are available for flow field simulation. Presently, four principal turbulence models are predominantly employed both locally and globally: k-ε (or RNG k-ε) model, Reynolds stress model (RSM), k-ω (or SST k-ω) model, and large eddy simulation (Rice) [33–35]. Given the unsteady, complex three-dimensional turbulent flow characteristics in the spiral-swirl separator for natural gas hydrate, this study employs the RNG turbulence model. This model accurately captures vortex-induced turbulence and viscous effects, while also ensuring a manageable computational load at low Reynolds numbers.

2.1.3. Multiphase Flow Modeling

The discrete phase model (DPM) was used to simulate particle motion within the separator, employing the particle random trajectory model to trace particle paths [36]. Particle collisions are not considered; instead, the focus is on the interactions between the fluid and particles. The governing equations for both phases are solved iteratively until convergence. Details of the equations for the axial, radial, and tangential components are provided as follows [37]:

$$\begin{cases} \frac{\mathrm{d}u_p}{\mathrm{d}t} = \frac{1}{\tau}\left(u_g + u_g' - u_p\right) - g \\ \frac{\mathrm{d}v_p}{\mathrm{d}t} = \frac{1}{\tau}\left(v_g + v_g' - v_p\right) + \frac{w_p^2}{r_o} \\ \frac{\mathrm{d}w_p}{\mathrm{d}t} = \frac{1}{\tau}\left(w_g + w_g' - w_p\right) - \frac{u_p w_p}{r_o} \end{cases} \tag{3}$$

where u_p, v_p, and w_p are the velocities of particles in different directions. τ is the relaxation time of particles.

Therefore, the particle relaxation time is as follows:

$$\tau = \frac{\rho_p d_p}{18\mu} \frac{24}{C_D Re_p} \tag{4}$$

2.2. Model Description

The in situ separation of hydrates under actual working conditions is highly complex. To manage the computational demands of a full simulation, the separator model is simplified. During gas hydrate extraction, the mixture includes gas hydrate, seawater, mud–sand, and additional impurities like seabed sediments. However, in the numerical simulation, only seawater, mud–sand, and gas hydrate are considered as primary phases. Given that the density of fragmented gas hydrate is similar to seawater and the hydrate particles are dispersed within the seawater, the mixture is treated as a continuous medium in the flow field simulation. To reduce computational complexity and eliminate extraneous variables, components such as the centering bracket and fixed ring are omitted, simplifying the model, as shown in Figure 1. The main geometric parameters of the spiral-swirl coupled in situ separator are shown in Table 1.

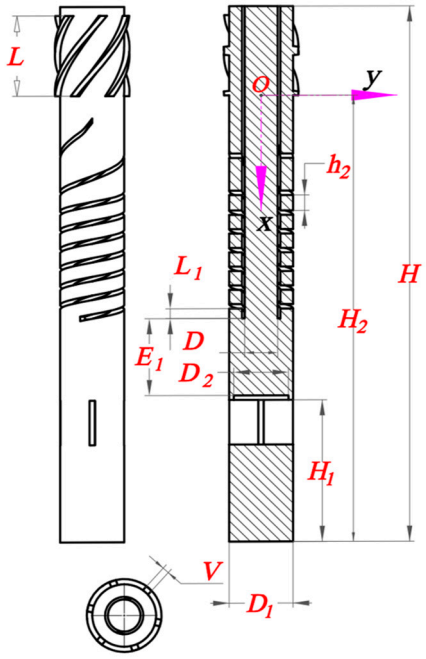


Figure 1. Schematic representation of the separator model and its flow channel geometry.

2.3. Boundary Conditions and Simulation Parameter Settings

The separator uses the inlet velocity magnitude as a boundary condition, determined from the known flow rate and inlet area. The outlet is set with a pressure boundary condition of 0.1 MPa. The fluid is modeled as a homogeneous mixture of seawater, natural gas hydrate, mud, and sand using the multiphase mixture model, with particle tracking handled by the discrete phase model (DPM). The SIMPLE algorithm facilitates pressure-velocity coupling, using a time step of 0.001 and 5000 iterations. Due to the high cyclonic flow and significant pressure gradients, the PRESTO scheme is applied for pressure discretization, and the Second Order Upwind scheme with QUICK format is used for convection. Additional parameters are outlined in Table 2.

Table 1. Structural parameters of spiral-cyclone in situ separator.

Parameters	Sign	Value
Total height of separator	H	1200 mm
Separator inner diameter	D_1	140 mm
Number of cyclone inlet guide ports	N_0	4
Cyclone inlet helical pitch	h_1	900 mm
Cyclone inlet helix turns	N_1	0.25
Cyclone inlet helix length	L	180 mm
Distance from the bottom of the cyclone inlet to the bottom of the separator	H_2	1000 mm
Spiral runner pitch	h_2	78 mm
Overflow pipe inner diameter	D	72 mm
Overflow pipe insertion length	L_1	0
Number of spiral turns of spiral runner	N_2	5.25
Vortex deflector position	E_1	136 mm
Sedimentation depth	H_1	317.5 mm
Vortex deflector diameter	D_2	120 mm

Table 2. Geometric parameters and operating conditions in numerical simulation.

Parameter	Value
Inlet velocity (m/s)	10
Inlet temperature (K)	273.15
Inlet turbulence intensity	5%
Outlet relative pressure difference (MPa)	0.1

Figure 2 shows the meshing process for the flow channel section in the spiral-cyclone separator. The channel is divided into 11 sections according to its geometry before meshing. A hexahedral mesh, chosen for its minimal computational error, is used to better capture parameter gradients within the separator. Local mesh refinement is also applied to enhance mesh quality and improve computational accuracy.

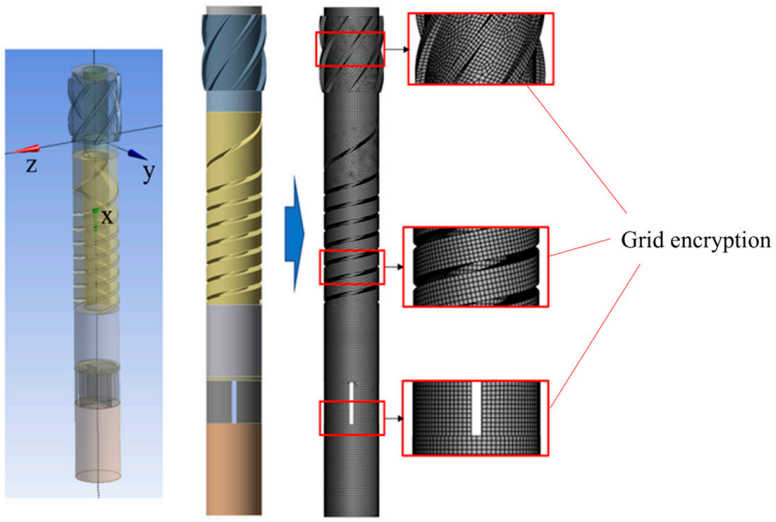


Figure 2. Geometric model meshing of the separator.

To verify the accuracy and reliability of the numerical simulation, it is necessary to simulate the separator with different grid sizes. In the separator simulation model, the mesh sizes of different sizes are 20 mm, 10 mm, 5 mm, and 2 mm, respectively. The numerical simulation results of the pressure drop of the first three sizes show that the errors

are 7.8%, 5.3%, and 1.6% of the maximum number of grids, respectively. It is generally considered that the error is allowed when the error is less than 5%. Therefore, to avoid the excessive number of grids seriously affecting the calculation speed, the grid size of 5 mm is taken for subsequent numerical simulation calculation under the premise of ensuring the calculation accuracy.

In terms of physical parameters, taking the natural gas hydrate core sampled by drilling in the Shenhu area of the South China Sea as an example, the sedimentary reservoirs of marine natural gas hydrate mainly include silt (4~63 μm, 67.043%) and clay (<4 μm, 28.74%). The physical parameters of each phase medium in the numerical simulation process are shown in Table 3.

Table 3. Physical property parameters of each phase medium.

Medium	Density (kg/m^3)	Particle (μm)	Viscosity (kg/(m·s))	Volume Fraction
Gas hydrate	910	50	1.2×10^{-5}	15
Solid particles (mud–sand)	2600	50	1.72×10^{-5}	20
Water	1030	-	1.7×10^{-3}	65

3. Simulation Analysis of Flow Field Characteristics

The in situ separator designed in this study utilizes a spiral-cyclone coupling principle for separation. The spiral-cyclone flow field is concentrated around the vortex deflector plate and between the spiral runner, where the separation of natural gas hydrate and silt sand particles occurs, along with the partial bond breaking of the hydrate. Thus, a detailed analysis of both the helical section and the cyclone region is essential. This area, as illustrated in Figure 3, extends from x = 500 mm to x = 650 mm in the x-direction. Cross-sections at x = 500 mm, 550 mm, 600 mm, and 650 mm are examined to assess the distribution of the velocity field, pressure field, sand phase, and hydrate phase within the spiral-cyclone separator.

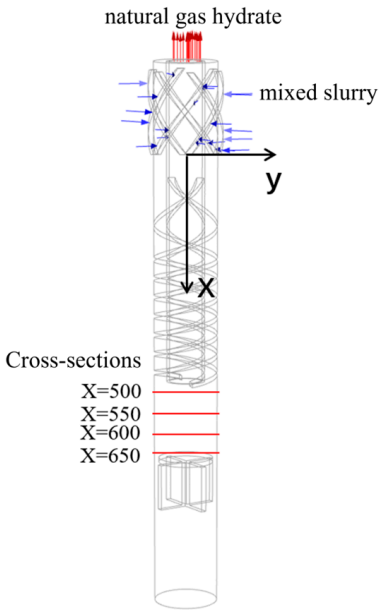


Figure 3. Schematic diagram of the cross-section location of the spiral-cyclone separator.

3.1. Verification of Particle Motion Trajectory

Verifying particle trajectories within the spiral-cyclone flow path is essential. This study uses the discrete phase model (DPM) with the Euler–Lagrange method to analyze these trajectories in the separator. As shown in Figure 4, the fluid efficiently separates gas hydrate and sediments between x = 500 mm and x = 650 mm, aligning with design specifications. The figure also indicates that density variations and the vortex deflector plate create two distinct cyclonic flows: an upward flow for intermediate-light fluids and a downward flow for heavy-phase fluids, driven by centrifugal forces. These findings confirm that the separator meets the design requirements for effective spiral-cyclonic flow trajectories.

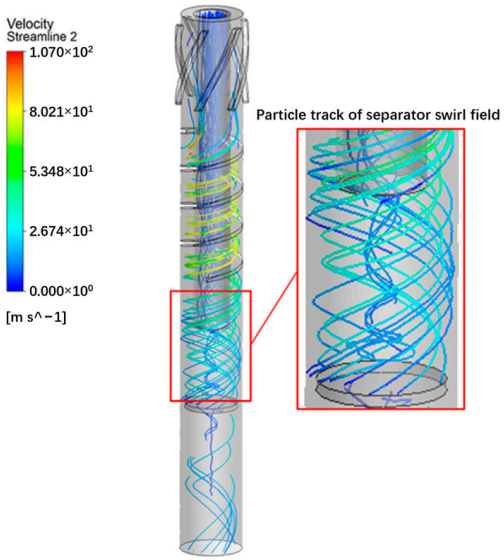


Figure 4. Particle trace diagram of the cyclone field of the separator.

3.2. Velocity Field

The magnitude of fluid velocity within the separator's field is crucial for determining separation efficiency. The characteristics of the flow field in the spiral-cyclone coupled separator play a significant role in its overall performance. Within the separator, the mixed slurry velocity can be broken down into axial, tangential, and radial components.

3.2.1. Mixed Slurry Velocity Distribution

The mixed slurry velocity reflects the fluid's overall movement within the separator, as shown in Figure 5. The cloud diagram highlights notable velocity variations in the spiral runner section, which generates a helical-cyclonic flow within the x-coordinate range of 500 mm to 650 mm. The relative velocity distribution curves at different radial cross-sections, also depicted in Figure 5, exhibit an 'M'-shaped symmetrical distribution. The slurry near the wall of the baffle can obtain a larger flow rate and then obtain a larger centrifugal force. Therefore, high-density mud–sand flows to the wall, and low-density natural gas hydrate flows to the center, realizing the separation of natural gas hydrate and mud–sand. Specifically, the slurry velocity is lower near the separator's axis and higher near the wall. Between radial positions of ±0.6 m and ±0.7 m, the velocity decreases sharply due to the wall's influence, with a significant reduction near the wall.

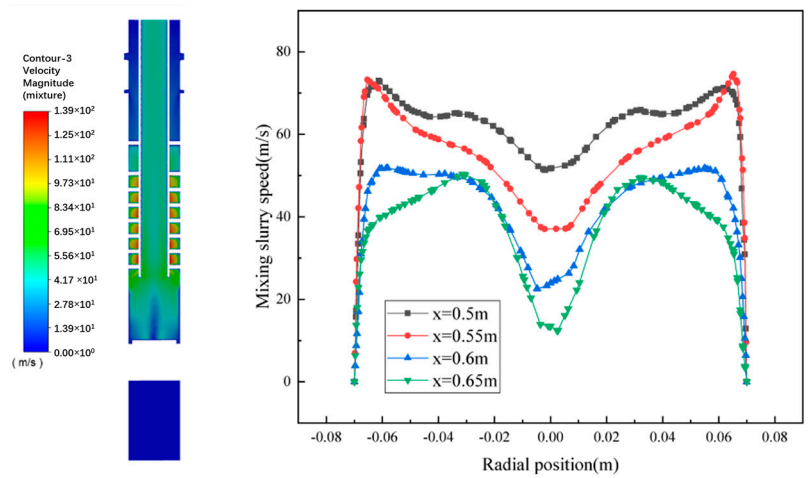


Figure 5. Velocity size distribution of mixed slurry.

3.2.2. Axial Velocity Distribution

The axial velocity indicates the fluid flow direction within the separator, as depicted in Figure 6. Positive values signify the inflow of mixed slurry into the separator, while negative values represent the outflow of purified natural gas hydrate from the central region. Analysis reveals that in the x-direction segment between 500 mm and 650 mm, the axial velocity increases as the distance from the wall decreases. Figure 6 supports this finding, showing that the axial velocity rises closer to the wall, which aligns with the observed separation and sedimentation of high-density mud and sand.

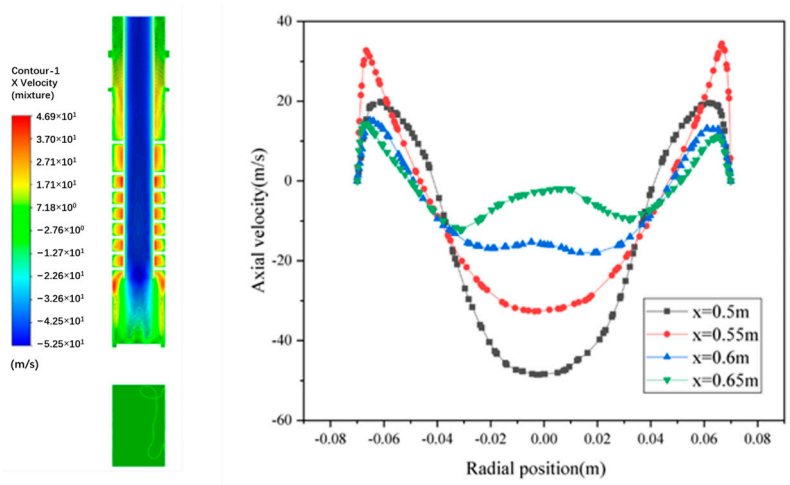


Figure 6. Axial velocity distribution of fluid inside the separator.

3.2.3. Radial Velocity Distribution

The radial velocity's magnitude reflects the fluid's movement relative to the separator's axis, with positive and negative values indicating direction. As shown in Figure 7, radial velocity experiences more significant fluctuations than tangential and axial velocities. Notably, in the x-direction region from 500 mm to 650 mm, these fluctuations are especially pronounced, highlighting substantial radial migration influenced by centrifugal force. Figure 7 also illustrates how radial velocity varies at x-coordinates of 500 mm, 550 mm, 600 mm, and 650 mm.

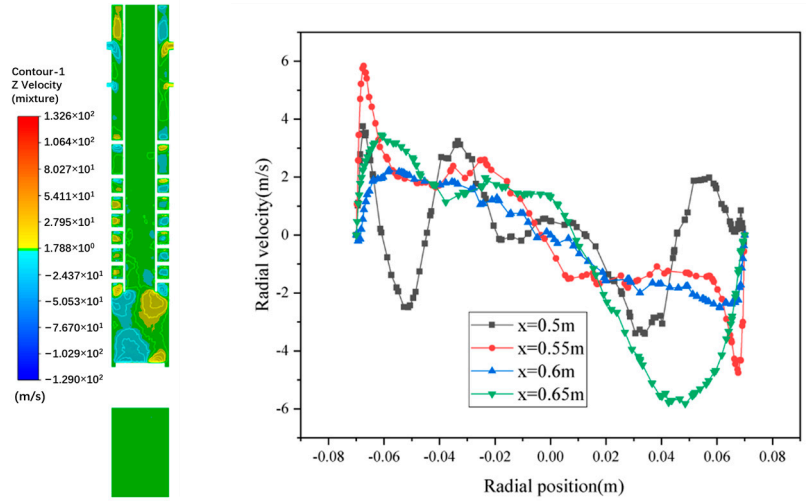


Figure 7. Radial velocity distribution of fluid inside the separator.

3.2.4. Tangential Velocity Distribution

Centrifugal force and tangential acceleration in the separator exhibit a quadratic relationship, with centrifugal force as the primary determinant of separation efficiency. The separator utilizes centrifugal separation driven by density variations, causing the separation medium to migrate radially outward from the center. Figure 8 reveals a pronounced gradient in the distribution of tangential velocity within the separator. The cloud diagram shows that positive and negative values represent the direction of tangential velocity, with the magnitude being greater near the walls and lower in the central region. Enhanced tangential velocity near the walls amplifies the centrifugal force on the mixed slurry, thereby increasing the separator's efficiency in separating sand from mud. The radial distribution curve of tangential velocity in Figure 8, at the x-coordinates of 500 mm, 550 mm, 600 mm, and 650 mm, shows that tangential velocity significantly exceeds radial and axial velocities, highlighting its essential role in separating natural gas hydrate from silt.

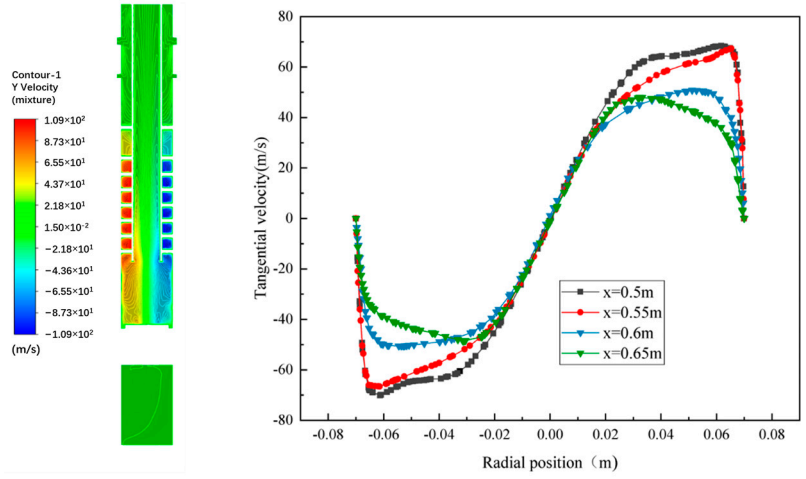


Figure 8. Fluid tangential velocity distribution inside the separator.

3.3. Pressure Field

Figure 9 illustrates that pressure rises with increasing distance from the central axis of the separator and decreases as one approaches the axis, sometimes leading to regions of negative pressure. During the separation process, static pressure aids in the transport of sediment and natural gas hydrate phases, while negative pressure regions induce an upward suction of hydrate and sediment particles. The static pressure distribution

curve presented in Figure 9 reveals an axisymmetric distribution across cross-sections at x-coordinates of 500 mm, 550 mm, 600 mm, and 650 mm.

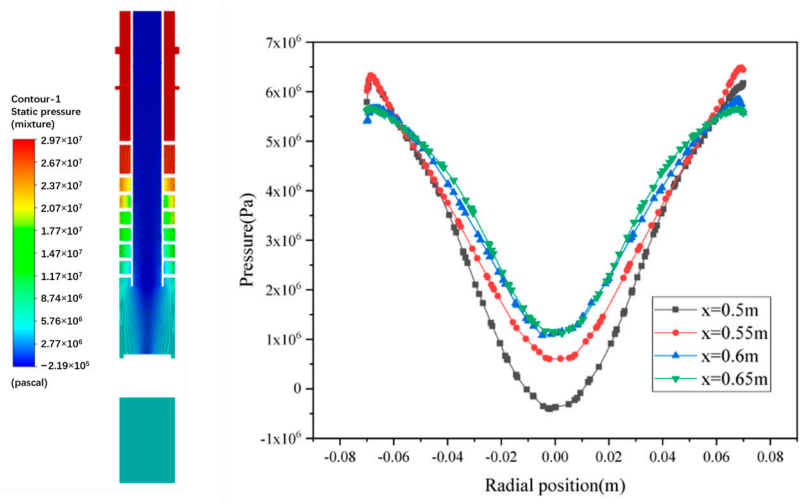


Figure 9. Separator static pressure distribution.

3.4. Sediment Phase Distribution

Figure 10 serves as a critical visual reference for evaluating the separator's efficiency in isolating heavy-phase silt. The silt distribution cloud diagram illustrates that a segment of the silt phase is segregated within the spiral runner area and concentrated along its wall due to centrifugal forces. Along the x-direction, across cross-sections from 500 mm to 650 mm, the separation of the silt phase is more distinct, with the silt descending along the wall. The silt phase distribution curve, depicted in Figure 10, demonstrates the dynamic behavior of the silt phase along the radial position within the separator. This flow field pattern is crucial for optimizing the separator in future applications. The observed distribution validates that the in situ separator developed in this study effectively segregates sediment from hydrate.

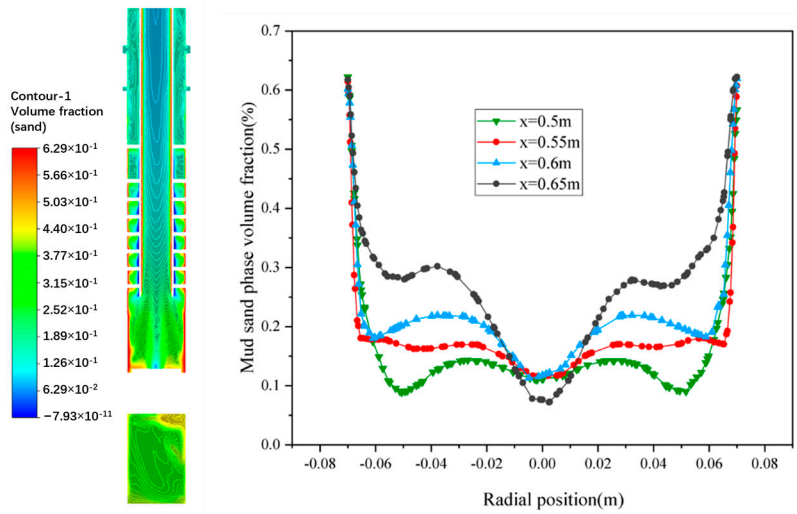


Figure 10. Sediment phase distribution in the separator.

3.5. Natural Gas Hydrate Phase Distribution

During the in situ separation of natural gas hydrate, analyzing the volume concentration of the hydrate reveals insights into the dynamic separation processes occurring within the separator. Figure 11 depicts the distribution of the hydrate phase volume fraction within the separator. The cloud diagram indicates that the hydrate phase adheres to the

movement pattern of the mixed slurry. Notably, the concentration of the hydrate phase exhibits substantial variation, particularly within the spiral flow channel and across the x-direction range of 500 mm to 650 mm. A notable cyclonic rise of the hydrate phase is observed in the central cross-sectional regions at x-coordinates of 500 mm, 550 mm, 600 mm, and 650 mm. Hydrates with smaller particle sizes and reduced densities are uplifted into the inner cyclone and subsequently transported to the sea surface through the overflow. The observed distribution of hydrate phases validates that the separator efficiently segregates the gas hydrate mixture slurry.

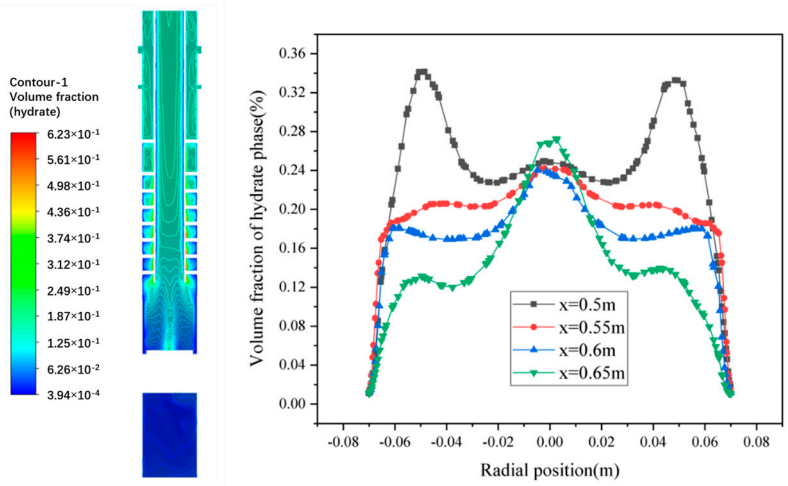


Figure 11. Hydrate phase distribution inside the separator.

4. Experimental Verification

4.1. Experimental System

The experimental system is shown in Figure 12. During the experiment, the mixed slurry enters the separator from the lateral inlet, and a flowmeter is set at the inlet. The separated mud–sand flows downward and settles at the bottom of the separator, and the purified hydrate flows upward and recycles from the overflow pipe. The design flow range of the pump is 25 m^3/h, and the volume concentration of the solid flow is between 5% and 15%.

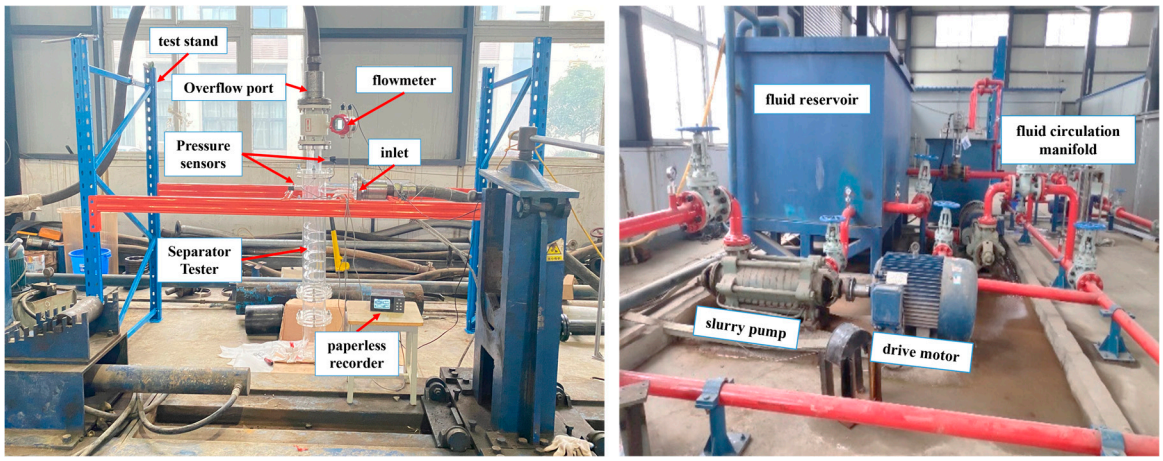


Figure 12. Experimental system diagram.

To facilitate the clear observation of the experimental phenomena in the spiral-cyclone in situ separator, the separator is made of high-strength Plexiglas (acrylic). Figure 13 shows the experimental prototype machining of the components; due to the separator using a split

design, only the geometric optimization needs to be processed separately, while the spiral flow channel, vortex deflector, cyclone inlet, separator shell, and sedimentation chamber, the other parts, do not have components that need to be optimized or changed and can be replaced.

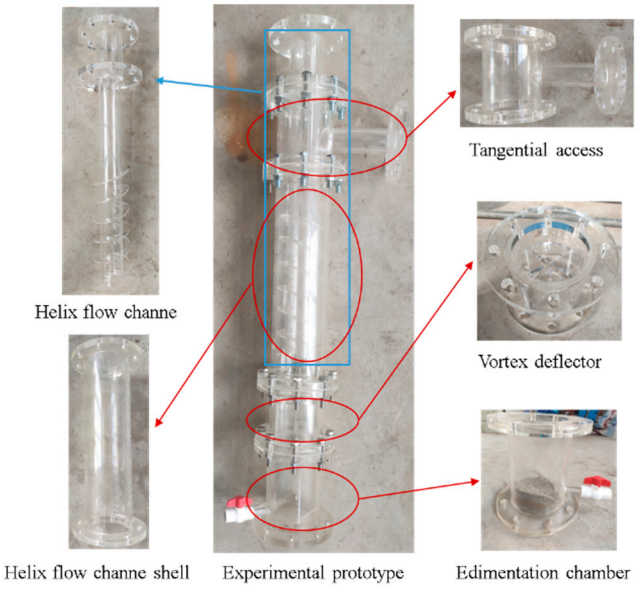


Figure 13. Physical drawing of each component of spiral-cyclone separator processing.

4.2. Comparison Validation

As shown in Figure 14, the experimental phenomenon of the overall separation process of the spiral-cyclone separator is compared with the simulation results. Because the indoor test cannot fully simulate the parameters such as temperature and pressure during the simulation, and the temperature and pressure fluctuate, the indoor experimental results are slightly different from the simulation. From the experimental phenomenon of the spiral-cyclone separator, we can find the difference in the transparency of the liquid in the hydrate recovery area and the sediment separation area, which is caused by the difference in the volume fraction of the sediment phase. This experimental phenomenon proves that the separator has the same separation effect as the numerical simulation from a macroscopic point of view, while the quantitative analysis of the separation efficiency of the separator needs to be determined by sampling the outlet and inlet fluids.

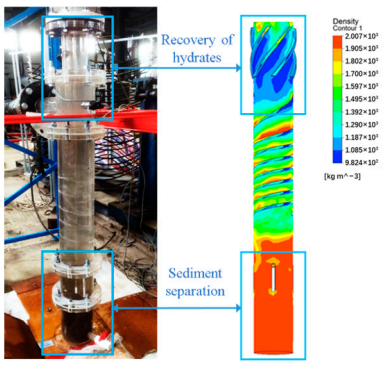


Figure 14. Comparison of experimental and simulation of the overall separation process of spiral-cyclone separator.

As shown in Figure 15, by comparing the numerical simulation and the indoor experimental phenomena, it is found that the volume fraction of the sediment phase is higher

at the wall of the separator, which is because the denser sediment is thrown to the wall of the separator under the action of the centrifugal force generated by the separator and the separation of the hydrate combined sediment is realized.

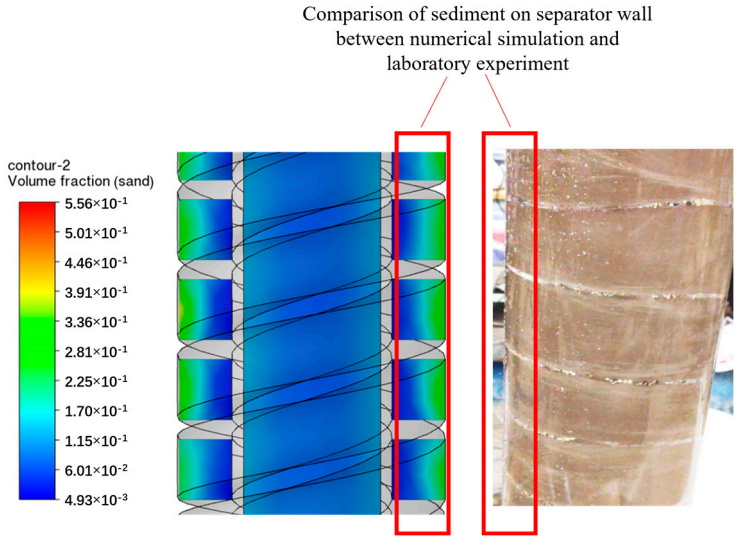


Figure 15. Local comparison between simulation and test.

Large particles in the separation by gravity are more obvious. To study the impact of large sand particles on the separation effect in the actual experimental process, with the addition of quartz sand, and also in the circulating water tank, a small amount of large-size sand particles with a particle size of about 1 mm was added in order to observe this in the separator at different operating attitudes. This was to discover whether the large size of the sand particles has an effect on the separation. As shown in Figure 16, when the separator is placed vertically, the experimental results and the simulation cloud show that the sand is separated and settles to the bottom of the separator. When the separator is placed parallel to the ground, a unilateral accumulation of sediment is formed due to the influence of gravity, but sediment also accumulates at the bottom of the separator. Therefore, the above two cases show that the separator has good performance in separating mud and sand at different operating postures.

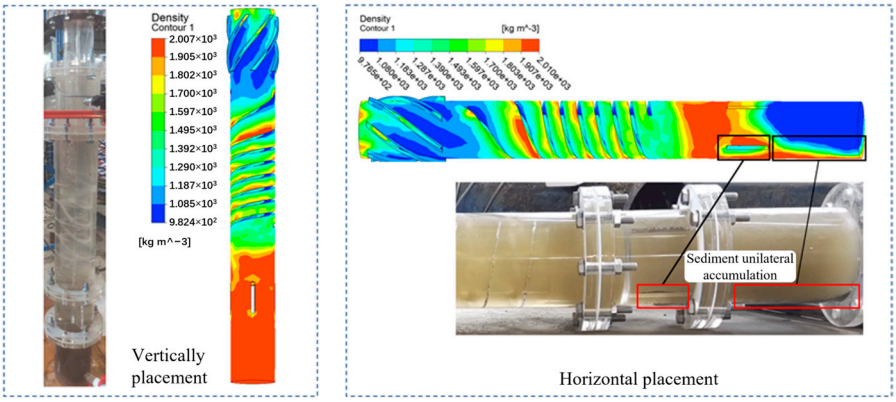


Figure 16. Comparison of experimental and simulated phenomena for different action attitudes of the separator.

5. Conclusions

In this study, in order to solve the problem of large amounts of sand being produced in the process of natural gas solid-state fluidization, a numerical simulation model of the

internal flow channel of the spiral-swirl in situ separator was established, and the flow field characteristics of this separator were verified and analyzed.

(1) Aiming to solve the problem of the low exploitation efficiency of natural gas hydrate caused by a large amount of sand production in the solid fluidization process of natural gas hydrate, the effective separation of natural water hydrate and mud–sand is realized.

(2) The numerical simulation of the internal flow field shows that the fluid velocity and pressure are axisymmetrically distributed, and the maximum value appears near the wall of the separator, which is beneficial to the separation of mud–sand and natural gas hydrate. Therefore, the inlet velocity and pressure can be appropriately increased.

(3) In the vicinity of the separator wall, the volume fraction of the sediment phase reaches the maximum value. In contrast, the volume fraction of the natural gas hydrate phase reaches the minimum value which verifies that the mud–sand with a higher density is dumped to the wall surface, indicating that the separation of mud–sand and natural gas hydrate has been realized.

(4) This study provides a new method for sand removal in natural gas hydrate mining. The designed spiral cyclone coupling separator has a great application prospect in the field of sand removal in hydrate mining.

Author Contributions: Y.H.: Writing—original draft, formal analysis, and conceptualization. X.J.: Writing—original draft, writing—review and editing. Y.T.: Visualization, validation, data curation, writing—review and editing. Y.Z.: Methodology, funding acquisition, writing—review and editing. N.X.: Project administration, validation. G.W.: Project administration, resources, and supervision. All authors have read and agreed to the published version of the manuscript.

Funding: This work was funded by the State Key Laboratory of Offshore Natural Gas Hydrate Open Fund Project [2022-KFJJ-SHW], the National Key R&D Program of China [2021YFC2800900], and the National Natural Science Foundation of China [U22244223].

Data Availability Statement: The original contributions presented in this study are included in the article. Further inquiries can be directed to the corresponding author.

Conflicts of Interest: Authors Yufa He and Yunjian Zhou were employed by CNOOC Research Institute Ltd. The remaining authors declare that the research was conducted in the absence of any commercial or financial relationships that could be construed as a potential conflict of interest.

References

1. Kezirian, M.T.; Phoenix, S.L. Natural Gas Hydrate as a Storage Mechanism for Safe, Sustainable, and Economical Production from Offshore Petroleum Reserves. *Energies* **2017**, *10*, 828. [CrossRef]
2. Qiu, S.Z.; Wang, G.R.; Wang, L.Z.; Fang, X. A Downhole Hydrocyclone for the Recovery of Natural Gas Hydrates and Desanding: The CFD Simulation of the Flow Field and Separation Performance. *Energies* **2019**, *12*, 3257. [CrossRef]
3. Sun, H.R.; Chen, B.B.; Yang, M.J. Effect of multiphase flow on natural gas hydrate production in marine sediment. *J. Nat. Gas Sci. Eng.* **2020**, *73*, 103066. [CrossRef]
4. Wei, N.; Pei, J.; Zhao, J.; Zhang, L.; Zhou, S.; Luo, P.; Li, H.; Wu, J. A state-of-the-art review and prospect of gas hydrate reservoir drilling techniques. *Front. Earth Sci.* **2022**, *10*, 997337. [CrossRef]
5. Koh, D.Y.; Kang, H.; Lee, J.W.; Park, Y.; Kim, S.J.; Lee, J.; Lee, J.Y.; Lee, H. Energy-efficient natural gas hydrate production using gas exchange. *Appl. Energy* **2016**, *162*, 114–130. [CrossRef]
6. Wang, J.Q.; Han, F.X.; Li, S.G.; Ge, K.; Zheng, Z.W. Investigation of gas hydrate production with salinity via depressurization and thermal stimulation methods. *J. Pet. Sci. Eng.* **2020**, *194*, 107465. [CrossRef]
7. Minagawa, H.; Ito, T.; Kimura, S.; Kaneko, H.; Noda, S.; Tenma, N. Depressurization and electrical heating of methane hydrate sediment for gas production: Laboratory-scale experiments. *J. Nat. Gas Sci. Eng.* **2018**, *50*, 147–156. [CrossRef]
8. Sun, H.R.; Chen, B.B.; Zhao, G.J.; Zhao, Y.C.; Yang, M.J. Utilization of water-gas flow on natural gas hydrate recovery with different depressurization modes. *Fuel* **2021**, *288*, 119583. [CrossRef]

9. Wang, B.; Fan, Z.; Wang, P.F.; Liu, Y.; Zhao, J.F.; Song, Y.C. Analysis of depressurization mode on gas recovery from methane hydrate deposits and the concomitant ice generation. *Appl. Energy* **2018**, *227*, 624–633. [CrossRef]
10. Feng, Y.; Chen, L.; Suzuki, A.; Kogawa, T.; Okajima, J.; Komiya, A.; Maruyama, S. Numerical analysis of gas production from reservoir-scale methane hydrate by depressurization with a horizontal well: The effect of permeability anisotropy. *Mar. Pet. Geol.* **2019**, *102*, 817–828. [CrossRef]
11. Ma, S.H.; Zheng, J.N.; Zhao, J.; Yang, M.J.; Song, Y.C. Experimental analysis on thermodynamic stability and methane leakage during solid fluidization process of methane hydrate. *Fuel* **2021**, *284*, 119020. [CrossRef]
12. Zhang, G.; Li, J.; Yang, H.; Liu, G.; Pang, Q.; Wu, T.; Huang, H. Simulation research on solid fluidization exploitation of deepwater superficial layer natural gas hydrate reservoirs based on double-layer continuous pipe. *J. Nat. Gas Sci. Eng.* **2022**, *108*, 104828. [CrossRef]
13. Wang, D.F.; Wang, G.R.; Zhong, L.; Liu, X.P. Effect of the protrusion of the mining chamber on particle recovery performance in solid-state fluidization mining for natural gas hydrate. *Geoenergy Sci. Eng.* **2024**, *233*, 212595. [CrossRef]
14. Yuan, S.; Sun, G.; Cao, G.; Wu, Y.; Yue, Y.; Song, Z. Study of the performance and flow field of a new spiral-roof cyclone separator. *Powder Technol.* **2024**, *438*, 119605. [CrossRef]
15. Sardar, R.; Oh, J.; Kim, M.; Lee, J.E.; Kim, S.; Kim, K.C. The effect of inlet velocity, gas temperature and particle size on the performance of double cyclone separator. *Chem. Eng. Process.-Process Intensif.* **2023**, *191*, 109469. [CrossRef]
16. Guzniczak, E.; Krüger, T.; Bridle, H.; Jimenez, M. Limitation of spiral microchannels for particle separation in heterogeneous mixtures: Impact of particles' size and deformability. *Biomicrofluidics* **2020**, *14*, 044113. [CrossRef]
17. Mihandoust, A.; Maleki-Jirsaraei, N.; Rouhani, S.; Safi, S.; Alizadeh, M. Improvement of size-based particle separation throughput in slanted spiral microchannel by modifying outlet geometry. *Electrophoresis* **2020**, *41*, 353–359. [CrossRef] [PubMed]
18. Saini, A.; Negi, A.S.; Kumar, A.; Chamkha, A.J. Radiative convective heat transfer and magneto-hydrodynamic flow in a viscous fluid-saturated porous channel with variable thermal conductivity. *Int. J. Ambient. Energy* **2024**, *45*, 2406908. [CrossRef]
19. Rawat, S.K.; Yaseen, M.; Pant, M.; Ujarari, C.S.; Joshi, D.K.; Chaube, S.; Negi, A.S.; Kumar, M. Designing soft computing algorithms to study heat transfer simulation of ternary hybrid nanofluid flow between parallel plates in a parabolic trough solar collector: Case of artificial neural network and particle swarm optimization. *Int. Commun. Heat Mass Transf.* **2023**, *148*, 107011. [CrossRef]
20. Negi, A.S.; Kumar, B. Nano-ferrofluid (Mn–Zn, $CoFe_2O_4$, Fe_3O_4) flow in a permeable channel with induced magnetic field. *Waves Random Complex Media* **2023**, *51*, 1–28. [CrossRef]
21. Tang, Y.; Li, Z.; Wang, G.; He, Y. A novel approach for nature gas hydrate separation: Downhole spiral-cyclone coupled hydraulic in-situ separation. *Chem. Eng. Res. Des.* **2022**, *188*, 808–822. [CrossRef]
22. Xie, B.; Li, S.; Jin, H.; Hu, S.; Wang, F.; Zhou, F. Analysis of the performance of a novel dust collector combining cyclone separator and cartridge filter. *Powder Technol.* **2018**, *339*, 695–701. [CrossRef]
23. Lan, W.; Wang, H.; Li, Y.; Feng, K.; Zhang, X.; Liu, Y.; Zhu, X.; Chen, S. Numerical and experimental investigation on a downhole gas-liquid separator for natural gas hydrate exploitation. *J. Pet. Sci. Eng.* **2022**, *208*, 109743. [CrossRef]
24. Nie, Q.; Zhang, S.F.; Huang, Y.; Yi, X.Z.; Wu, J.W. Numerical and Experimental Investigation on Safety of Downhole Solid-Liquid Separator for Natural Gas Hydrate Exploitation. *Energies* **2022**, *15*, 5649. [CrossRef]
25. Qiu, S.Z.; Wang, G.R. Effects of Reservoir Parameters on Separation Behaviors of the Spiral Separator for Purifying Natural Gas Hydrate. *Energies* **2020**, *13*, 5346. [CrossRef]
26. Chang, Y.L.; Ti, W.Q.; Wang, H.L.; Zhou, S.W.; Huang, Y.; Li, J.P.; Wang, G.R.; Fu, Q.; Lin, H.T.; Wu, J.W. Hydrocyclone used for in-situ sand removal of natural gas-hydrate in the subsea. *Fuel* **2021**, *285*, 119075. [CrossRef]
27. Duan, X.; Wu, J.; Huang, Y.; Lin, H.; Zhou, S.; Zhu, J.; Nie, S.; Wang, G.; Ma, L.; Wang, H. Achieving effective and simultaneous consolidation breaking and sand removal in solid fluidization development of natural gas hydrate. *Appl. Energy* **2023**, *351*, 121673.
28. Qiu, S.; Wang, T.; Wang, G.; Zhong, L.; Fang, X. Effect of Spiral Inlet Geometric Parameters on the Performance of Hydrocyclones Used for In Situ Desanding and Natural Gas Hydrate Recovery in the Subsea. *ACS Omega* **2023**, *8*, 5426–5436. [CrossRef]
29. Foroozesh, J. Computational fluid dynamics study of the impact of surface roughnesson cyclone performance and erosion. *Powder Technol.* **2021**, *389*, 339–354. [CrossRef]
30. Singh, H.; Kumar, S.; Mohapatra, S.K. Modeling of solid-liquid flow inside conical diverging sections using computational fluid dynamics approach. *Int. J. Mech. Sci.* **2020**, *186*, 105909. [CrossRef]
31. Islam, M.T.; Nguyen, A.V. Effect of particle size and shape on liquid–solid fluidization in a HydroFloat cell. *Powder Technol.* **2021**, *379*, 560–575. [CrossRef]
32. Heo, J.; Kim, K.D.; Kim, B.J. Improvement of One-Dimensional Two-Fluid Momentum Conservation Equations for Vertically Stratified Flow. *Nucl. Technol.* **2018**, *204*, 162–171. [CrossRef]
33. Sun, Z.P.; Liu, C.Y.; Yang, G.; Chen, L. Orthogonal vortices characteristic, performance evaluation and classification mechanism of a horizontal classifier with three rotor cages. *Powder Technol.* **2022**, *404*, 117438. [CrossRef]

34. Shastri, R.; Brar, L.S. Numerical investigations of the flow-field inside cyclone separators with different cylinder-to-cone ratios using large-eddy simulation. *Sep. Purif. Technol.* **2020**, *249*, 117149. [CrossRef]
35. Xu, M.H.; Yang, L.S.; Sun, X.H.; Wang, J.X.; Gong, L. Numerical analysis of flow resistance reduction methods in cyclone separator. *J. Taiwan Inst. Chem. Eng.* **2019**, *96*, 419–430. [CrossRef]
36. Li, H.; Song, Z.; Wang, R.; Sun, Z.; Zhang, A.; Zhang, X.; Si, H.; Hu, R.; Hu, Z. Study on the influence of baffle height and angle on the performance of coarse powder separator in power plant based on CFD-DPM method. *Int. J. Heat Fluid Flow* **2024**, *109*, 109523. [CrossRef]
37. Zhang, L.H.; Fan, J.L.; Zhang, P.; Gao, F.; Chen, G.H.; Li, J.L. Effect of local erosion on the flow field and separation performance of the cyclone separator. *Powder Technol.* **2023**, *413*, 118007. [CrossRef]

Disclaimer/Publisher's Note: The statements, opinions and data contained in all publications are solely those of the individual author(s) and contributor(s) and not of MDPI and/or the editor(s). MDPI and/or the editor(s) disclaim responsibility for any injury to people or property resulting from any ideas, methods, instructions or products referred to in the content.